Experimental validation of microwave imaging prototype and DBIM-IMATCS algorithm for bone health monitoring

Amin, Bilal; Shahzad, Atif; O'halloran, Martin; Mcdermott, Barry; Elahi, Adnan

DOI:
10.1109/ACCESS.2022.3167715

Document Version
Publisher's PDF, also known as Version of record

Citation for published version (Harvard):
Amin, B, Shahzad, A, O'halloran, M, Mcdermott, B & Elahi, A 2022, 'Experimental validation of microwave imaging prototype and DBIM-IMATCS algorithm for bone health monitoring', *IEEE Access*, vol. 10, pp. 42589-42600. https://doi.org/10.1109/ACCESS.2022.3167715

IEEE Access
Multidisciplinary ⋮ Rapid Review ⋮ Open Access Journal

Received March 22, 2022, accepted April 10, 2022, date of publication April 18, 2022, date of current version April 27, 2022.

Digital Object Identifier 10.1109/ACCESS.2022.3167715

Experimental Validation of Microwave Imaging Prototype and DBIM-IMATCS Algorithm for Bone Health Monitoring

BILAL AMIN[1,2], ATIF SHAHZAD[3,4], MARTIN O'HALLORAN[1,2], BARRY MCDERMOTT[1,2], AND ADNAN ELAHI[1,2], (Member, IEEE)

[1]Electrical and Electronic Engineering, National University of Ireland Galway, Galway, H91 TK33 Ireland
[2]Translational Medical Device Laboratory, National University of Ireland Galway, Galway, H91 TK33 Ireland
[3]School of Medicine, National University of Ireland Galway, Galway, H91 TK33 Ireland
[4]Centre for Systems Modelling and Quantitative Biomedicine, Institute of Metabolism and Systems Research, University of Birmingham, Birmingham B15 2TT, U.K.

Corresponding author: Bilal Amin (b.amin2@nuigalway.ie)

This work was supported by the European Research Council under the European Union's Horizon 2020 Program/ERC Grant BioElecPro under Grant 637780.

ABSTRACT The evaluation of the microwave imaging (MWI) prototype and imaging algorithms on experimental bone phantoms is a precursor step before clinical testing for measuring *in vivo* dielectric properties of human bones. To this end, this paper presents microwave tomographic image reconstruction of experimental phantoms of normal and diseased human calcaneus bone using an MWI prototype and distorted Born iterative method (DBIM) algorithm for bone health monitoring application. A two-layered simplified cylindrical-shaped 3-D printed phantom was used to mimic the human calcaneus bone. The external and internal layers of the bone phantom mimic the cortical bone and trabecular bone, respectively. Liquid tissue-mimicking mixtures (TMM) for normal bone, osteoporotic bone, and osteoarthritis bone were prepared. The phantoms were placed in the imaging prototype and the electromagnetic inverse scattering problem was solved using the DBIM to create the complex permittivity images. An L_2-based regularization approach was adopted along with the iterative method with adaptive thresholding for compressed sensing (IMATCS) to overcome the ill-posedness and to solve the underdetermined set of linear equations at each DBIM iteration. The reconstruction of dielectric properties of bone phantoms have shown that L_2-IMATCS approach provides a robust reconstruction of diverse bone phantoms with acceptable accuracy. Moreover, the osteoporotic and osteoarthritis bone phantoms were distinguished based on reconstructed dielectric properties with an average percentage difference of 26% at 3 GHz. This paper has made the first attempt to validate an MWI prototype for bone imaging application. A DBIM-based iterative method has been employed to classify normal and diseased bone phantoms.

INDEX TERMS Bone health, calcaneus bone phantom, dielectric properties, distorted born iterative method, microwave imaging.

I. INTRODUCTION

Osteoporosis is an important and significant bone disease resulting from a loss of minerals from the bone tissue and the resulting fragility giving an increased likelihood of fracture [1]. Indeed almost 8.9 million fractures annually are reported due to osteoporosis worldwide [2], with older patients more susceptible - 50% of the women and 20% of the men over the age of 50 years will suffer an osteoporosis-related bone fracture [3]. Current clinical practices widely employ dual-energy X-ray absorptiometry (DXA) for monitoring osteoporosis. But, due to the cumulative effect of repeated X-ray doses over time, the DXA scan poses long-term health risks [4]. Further, DXA does not offer any insight on bone quality which is dictated by the structure, tissue microarchitecture, composition, and the degree of microdamage, each of these are considered as important components towards bone health [3], [4]. Similarly, quantitative computed tomography (QCT) is rarely used in clinical practice due to the high-intensity X-ray doses (greater than 0.86 mrem), expensive equipment, and the cost of the test [5]. Therefore, there is a need for safer modalities for osteoporosis monitoring. Microwave imaging (MWI) is

The associate editor coordinating the review of this manuscript and approving it for publication was Amin Zehtabian.

a potential imaging modality that relies on the inherent dielectric contrast between healthy and diseased tissues of the target anatomical site in the human body [6]. The target anatomical site to monitor osteoporosis is trabecular bone [7]. Recent studies on dielectric measurements of the bones have found a notable dielectric contrast between healthy and diseased human trabecular bones indicating a potential role for MWI in monitoring pathology in this tissue [1], [9], [11]. MWI has made significant development towards the diagnosis of breast cancer [12]–[17] and brain stroke monitoring [18]–[20]. Various experimental prototypes have been developed for breast imaging and stroke detection, and some of these have been tested in clinical trials [21]. The key clinical advantages of MWI include non-ionizing radiations, portability, and low cost [1].

While MWI has been proposed to monitor osteoporosis based on the dielectric contrast between healthy and diseased human trabecular bones [9], [10], [22], no dedicated MWI system has been developed to measure *in vivo* dielectric properties of human bone in the microwave frequency range. To date, only two studies have measured *in vivo* dielectric properties of the human trabecular bones. Gilmore *et al.* [23] reported *in vivo* dielectric properties of the human forearms including bone by microwave tomography (MWT). The forearms of five healthy volunteers were imaged to evaluate the image reconstruction quality under the varying thickness of the arm's external adipose tissue layer. The authors found that without the use of prior information a thicker adipose tissue layer leads to a poorer image reconstruction quality. However, the image reconstruction quality has notable improvement when prior information is incorporated as an inhomogeneous background in the inversion algorithm. While the study demonstrated the successful reconstruction of *in vivo* dielectric properties of the bone, the relation between dielectric properties and bone health was not investigated. Meaney *et al.* [9] reported *in vivo* human heel imaging to assess the dielectric properties of calcaneus bone by using MWT. In this study, the human calcaneus of two patients (suffering from a lower leg injury) was imaged using a breast imaging prototype [9]. The study focused on the investigation of the correlation between the MWT images and corresponding bone mineral density (BMD) values. The (negative) correlation between the MWT images and BMD demonstrated by the authors indicates the potential of MWT for monitoring bone health. However, the study only considered two patients and results need to be further validated in a larger sample size. Despite promising initial results in the reconstruction of bone dielectric properties and evidence of the relationship between dielectric properties and bone health, no clinical MWI system has been developed for bone health monitoring. The authors have previously reported an experimental MWI prototype developed solely for calcaneus bone imaging [24], however, the prototype was not experimentally evaluated by imaging bone phantoms.

The focus of this study is to evaluate the imaging of different diseased bone phantoms using the experimental prototype to demonstrate the feasibility of MWI for use in monitoring osteoporosis. The contributions of this study include:

i) Development of different diseased bone phantoms,

ii) MWT reconstruction of the normal and diseased bone phantoms using the distorted Born iterative method (DBIM) approach and to assess its robustness and accuracy to image a simplistic two-layered bone structure,

iii) Distinguishing between osteoporotic and osteoarthritis bones based on the reconstructed dielectric properties.

To this end, three phantoms representing normal, osteoporotic, and osteoarthritis bone were developed. The trabecular bone microarchitecture of osteoarthritis patients is compact and dense compared to osteoporotic patients [10]. The dense trabecular microarchitecture of bone indicates a higher degree of mineralisation due to the greater amount of bone present. Therefore, the bone samples from osteoarthritis and osteoporotic patients allow establishing the variation in bone dielectric properties due to variation in mineralisation content and microarchitecture between two diseased bones [10]. The bone phantoms representing samples from these two sets of patients would incorporate variation in bone dielectric properties that would be representative of variation between healthy and diseased bones. The human calcaneus bone was modelled with an equivalent simplified two-layered three dimensional (3-D) printed cylinder. The calcaneus bone, in general, resembles an irregular shaped cylinder, therefore a cylindrical structure is a good approximation for initial imaging evaluation. The external layer of the cylindrical phantom constitutes the liquid tissue-mimicking mixture (TMM) for human cortical bone, whereas the inner layer constitutes the liquid TMM for human trabecular bone. Numerous studies have used 3-D printed breast and head models filled with liquid TMMs for MWI prototype testing [18], [20], [25], [26]. Recent advancements in manufacturing technologies have enabled building complex and relatively easily reproducible 3-D printed structures for use in phantom development. One drawback of 3-D printed moulds is the limited choice of fabricating substrates with acrylonitrile butadiene styrene (ABS) being the most commonly used. The ABS is commonly used despite its electrical permittivity and conductivity is far from the dielectric properties of biological tissues [27]. Therefore, the thickness of these 3-D printed structures should be kept as low as possible to minimize the effect it has on the microwave image [27]. This results in a balancing act between rigidity and low field perturbation. In the current study, the authors have tested ABS structures of 1.5 mm thickness and 2 mm thickness. The thickness of 2 mm for ABS structures ensured that the liquid TMMs do not leak to adjacent layers in a multi-layered 3-D printed structure and provides good mechanical stability. While liquid TMMs for cortical bone and normal trabecular bone have been previously reported by Amin *et al.* [24], TMMs for diseased trabecular bones particularly osteoporosis and osteoarthritis have not been previously reported in the literature. Therefore, new TMMs were developed to simulate the osteoporotic and osteoarthritis

conditions. These new TMMs were prepared by varying composition of trabecular bone to achieve the dielectric properties of osteoporotic and osteoarthritis trabecular bones, which have been reported by Amin *et al.* [10]. To scan these phantoms using the MWI prototype, a corresponding cylindrical-shaped 3-D printed phantom holder was designed. To acquire the microwave signals through the bone phantom antennas were mounted in the form of a circular array placed at equidistance to each other.

The acquired microwave signals were then used with the DBIM algorithm for the reconstruction of the dielectric profile of each phantom. The DBIM is a well-known linear approximation technique for solving the electromagnetic (EM) inverse scattering problem [28], [29]. Gilmore *et al.* [29] have used DBIM approximation to reconstruct the numerical leg phantom. However, the authors only considered cortical bone for leg imaging. Previously, Amin *et al.* [22] reported the reconstruction of numerical bone phantoms by employing the DBIM algorithm with an iterative method with adaptive thresholding for compressed sensing (IMATCS). While Amin *et al.* [22] has used the DBIM-IMATCS approach to reconstruct the numerical phantoms, this study has used the DBIM-IMATCS approach for the first time to reconstruct the experimental phantoms. Further, the EM inverse scattering problem is approximated as linear during the reconstruction process, therefore, the IMATCS algorithm may diverge after some iterations. To address this limitation, an L_2-regularization strategy is employed that leads to stable signal recovery [30].

To quantitatively evaluate the reconstructed tomographic images, most of the previous studies have only used normalized root mean square error (NRMSE) as a performance metric [20], [21], [32]–[34]. The NRMSE computes the difference between two images pixel-by-pixel. The difference is summed and normalized over all pixels. Therefore, it becomes difficult to differentiate between pixels that have higher error values compared to pixels that have lower error values. To address this limitation this study has also used the structural similarity index (SSIM) as an additional performance metric. The SSIM compares two images based on spatially near-pixels [15]. The SSIM reflects the similarity between reference and reconstructed images based on the luminance, contrast, and structure of images. To further evaluate the reconstructed images pixel-by-pixel this study has created histograms of reconstructed images. The reconstructed images having a large number of pixels close to the reference value are considered better images. The adoption of three-dimensional quantitative analysis helps to thoroughly compare the reference and reconstructed images. The proposed liquid TMMs are characterized over a frequency range of 1.5 – 4.5 GHz. Further, the average percentage difference between the relative permittivity of reference data and proposed liquid TMMs was found to be less than $\pm 10\%$. However, a slightly more deviation has been observed for the conductivity values. The findings on the evaluation of the MWI prototype and DBIM based MWT imaging algorithm have demonstrated that the bone phantoms can be reconstructed with acceptable accuracy. Moreover, the reconstructed complex permittivity images are good enough to distinguish between healthy and diseased bone phantoms. This two-layered 3-D printed cylindrical bone phantom and imaging prototype can be used as a tool for pre-clinical assessment of calcaneus bone imaging.

The remainder of the paper is organized as follows: Section II discusses the methodology for the preparation of calcaneus bone phantom and the preparation of liquid TMMs, dielectric characterization of liquid TMMs, the imaging prototype, a summary of DBIM and L_2-IMATCS approach, the simulation scenario, and the performance metrics to evaluate the reconstructed images. Section III discusses the results of dielectric properties of liquid TMMs and dielectric properties of reconstructed experimental bone phantoms. Finally, conclusions and future work are presented in Section IV.

II. METHODOLOGY

A. PREPARATION OF CALCANEUS BONE PHANTOM AND LIQUID TMMs

This study used the two-layered hollow cylinder model previously presented by Amin *et al.* [6] to mimic the human calcaneus bone as shown in Figure 1. As the anatomy of the calcaneus bone resembles an extended cylinder, a hollow cylinder model is a reasonable approximation. The dimensions of the inner chambers of the calcaneus model were designed to mimic the dimensions of the cortical and trabecular bone layers of the calcaneus bone [34], [35]. The thickness of the cortical bone was kept at approximately 6 mm, whereas, the trabecular bone was modelled with a thickness of 44 mm to ensure the maximum penetration of the EM field. Moreover, motivation for the use of the human calcaneus was due to the similar cortical to the trabecular ratio of that bone to that found in the femoral head and lumbar spine [34], [35] which are considered as primary targets for monitoring osteoporosis. The 3-D cylindrical models were produced using the Autodesk Fusion 3D software package, with these computational models then printed using an Ultimaker 2+ Extended 3-D printer at 200 °C using a polylactic acid (PLA) filament. Next, the outer and inner layers of the hollow cylinder were filled with cortical bone and trabecular bone liquid TMM respectively. To prevent the leakage of liquid TMM material the cylinder wall thickness was set at 2mm.

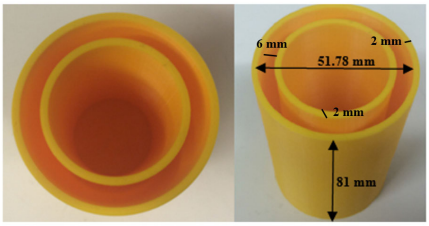

FIGURE 1. 3-D printed cylindrical calcaneus bone structure (a) Top view (b) Side view.

The methodology for the preparation of liquid TMMs has been outlined by Amin *et al.* [6]. The solution of Triton X-100, deionized water, and salt (NaCl) was put in a glass beaker and was thoroughly mixed until the disappearance of air bubbles. While liquid TMMs for normal bone have been previously reported by Amin *et al.* [24], TMMs for diseased bones particularly osteoporosis and osteoarthritis have not been previously reported in the literature. Therefore, this study presents the liquid TMMs for osteoporotic and osteoarthritis human trabecular bones. The composition of constituents was adjusted until the dielectric properties of TMMs were close to the reference values of osteoporotic and osteoarthritis bones reported by Amin *et al.* [10]. The recipe for cortical bone and trabecular bone TMM was obtained from Amin *et al.* [24]. The composition of TMMs that mimic the dielectric properties of each target tissue is given in Table 1.

TABLE 1. Composition of liquid TMMs.

Target Tissue	TX-100 (vol %)	DI water (vol %)	NaCl (g/L)
Cortical Bone [24]	77	23	0.8
Normal Trabecular Bone [24]	69.5	30.5	0.8
Osteoporotic Trabecular Bone	72.70	27.30	0.8
Osteoarthritis Trabecular Bone	65	35	0.8

TX = Triton X, DI = Deionized water. The quantity of NaCl is expressed in terms of grams/litre (g/L).

This study considers a total of three bone phantoms. The outer layer in all phantoms contains liquid TMM of the cortical bone. The inner layer that mimics the trabecular bone was varied to account for the natural pathological changes seen in the clinical conditions (osteoporosis and osteoarthritis) compared to the normal trabecular bone as reported by Amin *et al*. [10]. The sequence of bone tissues for outer and inner layers with their corresponding labels are tabulated in Table 2.

TABLE 2. Experimental bone phantoms.

Phantom Label	Outer Layer TMM	Inner Layer TMM
P1	Cortical Bone	Normal Trabecular Bone
P2	Cortical Bone	Osteoporotic Trabecular Bone
P3	Cortical Bone	Osteoarthritis Trabecular Bone

These antennas have been previously used for breast imaging studies [13], [15], [36], and authors have reported that the optimal reconstruction was found at 3 GHz. Therefore, the reconstruction of dielectric properties of all experimental bone phantoms was performed at 3 GHz, the other frequency points were not considered for the reconstruction of dielectric properties. To this end, the proposed TMMs were prepared for 3 GHz frequency. The relative permittivity and conductivity of the proposed TMMs at 3 GHz are tabulated in Table 3.

TABLE 3. The relative permittivity and conductivity for liquid TMMs at 3 GHz.

Target Tissue	ε_r	$\sigma(S/m)$
Cortical Bone	9.93	0.78
Normal Trabecular Bone	17.60	1.02
Osteoporotic Trabecular Bone	16.59	1.24
Osteoarthritis Trabecular Bone	25.19	1.50

B. DIELECTRIC CHARACTERIZATION OF LIQUID TMMs

Dielectric characterization of the liquid TMMs was performed using an open-ended coaxial probe (OECL) over the frequency range of 1.5 – 4.5 GHz. A Keysight slim form probe 85070E was connected directly to the Keysight E5063A vector network analyzer (VNA) [37]. The measurement equipment was first calibrated using a standard three-load one-port calibration (air, short, and deionized water). To verify the calibration, the dielectric properties of the 0.1 M NaCl solution (saline) were measured at 22 °C, with the saline acting as a reference material [38]. The uncertainty of the accuracy of the equipment is reported in Table 4 and is defined as:

$$ACC_{UC}(f) = \left(\frac{y_{meas}(f) - y_{ref}(f)}{y_{ref}(f)}\right) \times 100 \qquad (1)$$

where y_{meas} and y_{ref} represents the measured and reference dielectric properties of 0.1 M NaCl respectively [38], and f represents frequency. Table 4 also reports the uncertainty in repeatability of measurements, with this defined as:

$$REP_{UC}(f) = \left(\frac{y_{meas}(f) - y_{mean}(f)}{y_{mean}(f)}\right) \times 100 \qquad (2)$$

where y_{mean} represents the mean of the measured dielectric properties. The y_{mean} is calculated by taking the mean of 6 measurements. Finally, the total combined uncertainty which is the sum of ACC_{UC} and REP_{UC} is also reported in Table 4.

TABLE 4. Percent uncertainty in accuracy and repeatability of measurements.

Parameter	ε_r (%)	σ (S/m) (%)
UC_{ACC}	0.12	3.56
UC_{REP}	0.04	0.01
Combined	0.16	3.57

C. MICROWAVE SCANNING OF THE PHANTOMS

The imaging prototype was designed by modifying the cylindrical model. The height of the imaging tank was 82 mm, whereas the overall width was 54 mm. A total of six holes were fabricated in a plane in a radial pattern to house the flexible microstrip antennas [15]. These antennas have been previously used in a 16-element antenna array with patients for breast imaging applications [13], [15], [36]. In earlier breast imaging studies, these antennas were designed to contact the skin directly [13], [15], [36], hence no matching medium was used. In this study the skin layer was not

included in the bone phantoms, therefore, a mismatch at the first interface has been observed. The inclusion of a skin layer in future phantom will reduce the mismatch and will further improve the reconstructed images. The microwave signals from the antenna array were measured by a 2-port ZNB40 VNA and ZN-Z84 24-port switching matrix (Rohde and Schartz GmbH, Munich, Germany). Hence, the imaging prototype was composed of these 6 flexible microstrip antennas placed equidistant to each other. An overview of the experimental setup is shown in Figure 2. The VNA and the MWI prototype were not moved during the whole measurement procedure. This is achieved by raising the MWI prototype on a lift table and acquiring measurements until repeatable results are obtained. The signals were collected in the frequency range of 1.5 – 4.5 GHz as this is the optimal frequency range for the operation of the antennas with this system [15]. As the imaging prototype is composed of six antennas, a total of fifteen measurements ($N(N-1)/2$, where N denotes the number of antennas) were recorded that included the unique measurements from each transmit-receive antenna pair. The redundant data from reciprocal channels and monostatic channels was not recorded. The input power of the VNA was set to 0 dBm.

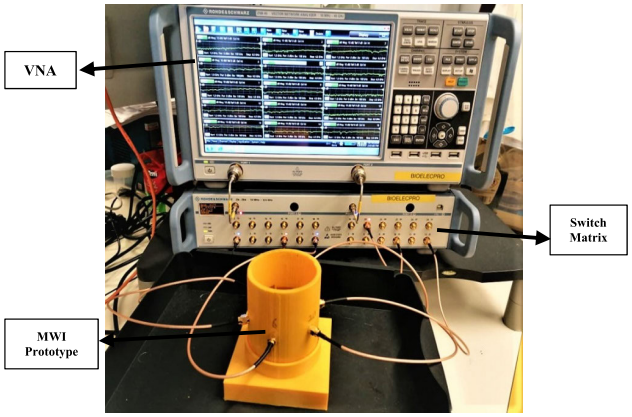

FIGURE 2. Realization of a 3-D MWI system prototype. A VNA is connected to a switching matrix. The switching matrix is connected to the cylindrical imaging prototype through cables.

D. IMAGE RECONSTRUCTION USING DBIM FORMULATION AND IMATCS ALGORITHM

The EM inverse scattering problem is ill-posed and non-linear as the number of measurements is less than the number of unknowns [39]. The dielectric properties of the target region from the measured EM scattered fields are computed by an EM simulation using an inversion of a linear approximation of the EM field [39]. More precisely, this study used the DBIM approximation proposed by Chew and Wang [40]. During each DBIM iteration, the EM scattering wave equation is linearized by replacing the total field with a known incident field which is estimated in the presence of known background [41]. The integral equation of EM field at measurement point r' and frequency ω can be expressed as:

$$\Delta E_s\left(r_T, r_R, \omega\right) = E_t\left(r_T, r_R, \omega\right) - E_b\left(r_T, r_R, \omega\right) \quad (3)$$

$$= \omega^2 \mu \int_V G_b\left(r', r_R, \omega\right) \delta\left(r', \omega\right) E_t\left(r', r_T, \omega\right) dr', \quad (4)$$

where ΔE_s is the scattered field due to the unknown contrast function $\delta\left(r', \omega\right)$ in volume V, E_t is the unknown total field, E_b is the background field, G_b is the dyadic Green's function which denotes propagation from the source located at $r' \in V$ to r_R, r_T and r_R representing the transmitter and receiver locations, and ω represents the angular frequency.

To find the *inverse solution*, this study has employed the IMATCS method [30]. The IMATCS method employs an adaptive threshold approach. The initial threshold value is exponentially decreased at each iteration of the IMATCS algorithm. The measurements in Eq. (4) are not linear which leads to instability and divergence of IMATCS iterations. To overcome this problem, an L_2-regularized approach is adopted [30]. The L_2-IMATCS method can be expressed as:

$$\mathrm{x}_{k+1} = \frac{1}{1+\beta_2} Th_0 e^{-\alpha i}\left(\mathrm{x}_k + \beta_1 \mathrm{A}^*\left(\mathrm{y} - \mathrm{A}\mathrm{x}_k\right)\right) \quad (5)$$

where Th_0 is the initial threshold, A^* is the conjugate transpose of measurement matrix, β is the relaxation parameter and controls the convergence, x_k is the unknown vector, α denotes the threshold step size, and i is the iteration number. The initial value of x_k in Eq. (5) starts with zero. The x_k is recovered after the specified number of IMATCS iterations. β_1 and β_2 controls the convergence of the algorithm. The L_2-IMATCS approach provides a stable and better recovery of x_k from measurements given in Eq. (4).

E. FDTD MODELLING AND CALIBRATION OF MEASURED DATA

The measured data was collected from the imaging prototype composed of 6 flexible microstrip antennas. The scattered EM signals from the bone phantoms were recorded. To perform the numerical simulation a similar imaging model was developed as used in the experimental setup. However, the antennas used in the numerical setup are not realistic. A total of six ideal dipole antennas were placed in a circular array. For the two-dimensional (2-D) geometry, the dipole antennas correspond to point sources. The finite-difference time-domain (FDTD) method was used to perform the numerical simulations. The initial guess for the DBIM inversion assumes that the imaging region is composed of the homogenous background medium $\varepsilon_\infty = 2.848$, $\Delta\varepsilon = 1.104$, $\sigma_s = 0.005\ S/m$ [30]. To simplify the FDTD simulation, the relaxation time constant was considered spatially invariant with a constant value of 0.5 ps. Further, no a-priori information regarding the shape of the target was used for the inversion procedure. The evaluated bone phantoms, simulations, and reconstructions are performed for 2-D imaging scenarios. The L_2-IMATCS approach reconstructs the single-pole Debye parameters

which were then converted into a complex permittivity profile of bone. The solution of the inverse problem relies on the comparison between the measured experimental data and the simulated scattered EM field data [42], [43]. The FDTD 2-D numerical model is not perfect in comparison to the experimental model due to the use of non-realistic antennas during the inversion procedure. Due to the use of non-realistic antennas in the numerical model, the reconstruction process is prone to propagation and scattering errors. Further, it is often challenging to incorporate a realistic antenna in the numerical model which requires specialized antenna modelling software and increases computations. However, calibration is a straightforward and robust method to mitigate such errors [32]. Therefore, before the inversion of EM scattered field data, a calibration of the measured data was performed as follows:

$$E^m_{cal}(f) = \left(\frac{S^m_{scat}(f)}{S^m_{ref}(f)}\right) E^s_{ref}(f) \tag{6}$$

where $S^m_{scat}(f)$ represents the measured transmission coefficients in the presence of the test object, $S^m_{ref}(f)$ represents the measured transmission coefficients in the absence of test object, and $E^s_{ref}(f)$ is the corresponding simulated reference signal. During the reconstruction process $E^m_{cal}(f)$ is used for comparing with the scattered field data from FDTD simulations [42], [43].

F. EVALUATION OF RECONSTRUCTED IMAGES

To quantitatively evaluate the reconstructed images of bone phantoms this study has considered NRMSE, SSIM, and histogram-based analysis. The histogram-based analysis is the novel analysis proposed in this study to address the limitations of NRMSE and SSIM as described in Section I.

1) ***Normalized Root Mean Square Error:*** The NRMSE computes the error between the complex permittivity of reference bone phantom and reconstructed bone phantom. The NRMSE is the standard metric used to evaluate the reconstructed phantoms as reported in the literature [18], [20], [32], [44]. The NRMSE is defined as:

$$\text{NRMSE} = \frac{\| \varepsilon_r(f) - \hat{\varepsilon}_r(f) \|^2_{\text{L}^2}}{\| \varepsilon_r(f) \|^2_{\text{L}^2}} \tag{7}$$

where $\varepsilon_r(f)$ is the complex permittivity profile of reference bone dielectric properties and $\hat{\varepsilon}_r(f)$ is the complex permittivity profile of reconstructed bone dielectric properties. The NRMSE values range between 0 and 1, a value of 0 indicates no error, however, a value of 1, indicates maximum error between two images under comparison. The NRMSE is separately calculated for both the real (ε') and imaginary (ε'') parts of complex permittivity profile for all bone phantoms.

2) ***Structural Similarity Index:*** The SSIM computes the correlation between the reference and reconstructed bone dielectric properties [15]. The correlation is computed based on the luminance, contrast, and structure between the reference and reconstructed images. The SSIM values range between 0 and 1. A value of 0 reflects no structural similarity and a value of 1 reflects the maximum similarity between two images. The SSIM is separately calculated for both the real and imaginary parts of the complex permittivity profile for all bone phantoms.

3) ***Histogram-based Analysis:*** While NRMSE and SSIM provide a good estimate of the quality of reconstruction, these metrics do not provide insight into pixel-wise error between the reference and reconstructed images. Therefore, to compare the distribution of reconstructed pixels of bone phantoms with corresponding pixels of reference bone phantoms this study has proposed a novel histogram-based analysis as an additional performance parameter. The histogram of reconstructed pixels was created. The reconstructed images having histogram distribution with a large number of pixels close to corresponding reference value are considered better images. The histogram analysis provided an additional tool to evaluate the accuracy of reconstructed images.

III. RESULTS AND DISCUSSION

This section presents the dielectric properties of liquid TMMs developed to mimic different types of bones. Moreover, the results obtained by L_2-IMATCS approach for bone dielectric properties reconstruction using dielectrically informed experimental bone phantoms are also presented in this section.

A. DIELECTRIC PROPERTIES OF LIQUID TMMs

The liquid TMMs were made to mimic the dielectric properties of cortical bone, trabecular bone, osteoporotic bone, and osteoarthritis bone. While the recipe for cortical bone and trabecular bone was obtained from Amin *et al.* [24], the recipe for osteoporotic and osteoarthritis was developed in this study as described in Section 2. The dielectric properties of all TMMs were analyzed. The composition of TMMs that mimic the dielectric properties of each target tissue is given in Table 1.

The dielectric properties of liquid TMMs and the corresponding reference dielectric data are shown in Figure 3. The solid lines represent the dielectric properties of liquid TMMs and the dashed lines represent corresponding reference dielectric data. The solid lines in Figure 3 indicate the mean value of six measurements taken between 1.5–4.5 GHz. The reference dielectric data for normal human cortical bone and trabecular bone was taken from Gabriel *et al.* [45]. The reference dielectric data for human osteoporotic bone and human osteoarthritis bone was taken from Amin *et al.* [10]. It can be observed from Figure 3 (a) and (b), that the mean dielectric properties of all TMMs are well aligned with the reference dielectric properties of modelled tissues and maintain a significant dielectric contrast to each other.

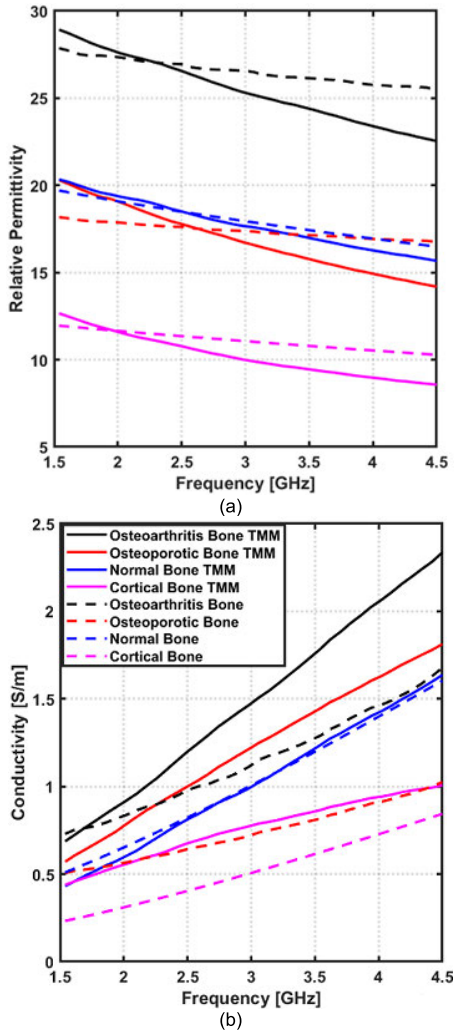

FIGURE 3. Dielectric properties of liquid TMMs over 1.5 – 4.5 GHz frequency band: (a) Relative Permittivity (b) Conductivity. The measured dielectric data of TMMs (solid lines) are compared with reference data (dotted lines) from Gabriel *et al.* [45] and Amin *et al.* [10].

The average percentage difference between the overall relative permittivity of the TMMs and corresponding reference tissues is observed as less than $\pm 10\%$, which is inside the expected variance in biological tissue [6]. The relative permittivity of liquid TMMs shows very good agreement with the reference data compared to the conductivity values. However, there is a relatively large deviation between the conductivity of liquid TMMs and reference data specifically for osteoporotic bone and osteoarthritis bone TMMs. This large deviation is mainly observed due to the presence of a high amount of deionized water in these TMMs and the variations observed (both in relative permittivity and conductivity) agree with the literature reporting TMMs for human biological tissues [20], [25], [46], [47]. The proposed TMMs maintain a realistic contrast between the conductivities of target bone tissues. Moreover, MWT relies on the contrast in relative permittivity, therefore, the variations observed in conductivity values are not critical to this specific investigation.

B. RECONSTRUCTION OF EXPERIMENTAL BONE PHANTOMS P1, P2, AND P3

The two-layered 3-D printed calcaneus structure was placed in the imaging prototype shown in Figure 2. The scattered EM signals from all 6 flexible microstrip antennas were measured. These EM signals were used to reconstruct the complex permittivity profile at 3 GHz. The FDTD simulation was used as a forward solver for the inversion process with a uniform grid cell size of 1 mm. The choice of the number of IMATCS iterations, DBIM iterations, and threshold Th_0 was based on the parametric analysis. The minimum value of NRMSE was obtained for five IMATCS iterations. Regarding the DBIM iterations, the minimum value of NRMSE was observed for the first DBIM iteration. Therefore, the reconstruction of all bone phantoms in this study was obtained for the first DBIM iteration. The value of the threshold was kept in the range of 2 – 3 for the reconstruction of all considered bone phantoms. For bone phantoms P1, P2, and P3, the external layer of the 3-D printed calcaneus structure was composed of liquid TMM for human cortical bone. The numerical equivalent models representing reference real and imaginary parts of the complex permittivity were developed as shown in Figures 4(a) and (b), 5(a) and (b), and 6(a) and (b) for the bone phantoms P1, P2, and P3 respectively. The outer layer in all numerical equivalent models mimics the cortical bone, whereas the inner yellow layer mimics the human trabecular bone for P1, human osteoporotic bone for P2, and human osteoarthritis bone for P3.

For the bone phantom P1, the internal layer of the 3-D printed calcaneus structure was filled with the liquid TMM of human trabecular bone. The dielectric contrast between cortical bone and trabecular bone is low, due to which reconstructing the dielectric profile of a two-layered bone structure by employing MWT is challenging. To this end, a DBIM based MWT imaging algorithm along with L_2-IMATCS approach was chosen to reconstruct the complex permittivity profiles of bone phantoms. The DBIM algorithm is known to be effective for reconstructing low contrast imaging scenarios, therefore, one of the objectives of this study was to assess the robustness and accuracy of the DBIM approach to image a two-layered bone structure. The reconstructed real and imaginary parts of complex permittivity of bone phantom P1 are shown in Figure 4(c) and (d) respectively. Comparing the reference and reconstructed real and imaginary parts of the complex permittivity profiles, it can be observed that the reconstructed profiles have a relatively low error at the region of interest (central trabecular bone region) in the reconstructed image. While the shape is not perfectly preserved in reconstruction, it is evident from the reconstructed images that both layers have been reconstructed. The artefacts are prominent at the boundary of the imaging domain as expected. These artefacts can be attributed to EM field perturbation at the boundaries of two mediums with different dielectric properties.

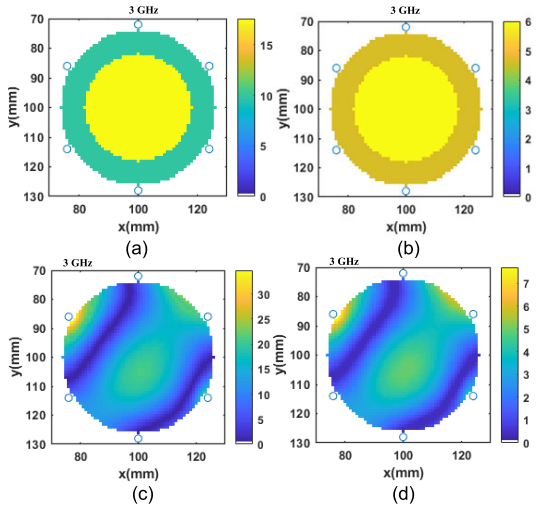

FIGURE 4. Real and imaginary parts of complex permittivity at 3 GHz of (a) and (b) reference bone phantom P1, (c) and (d) reconstructed bone phantom P1.

For the bone phantom P2, the internal layer of the 3-D printed calcaneus structure was filled with the liquid TMM of human osteoporotic bone. The reference dielectric data for human osteoporotic bone was obtained from Amin *et al.* [10]. The reconstructed real and imaginary parts of complex permittivity of bone phantom P2 are shown in Figure 5(c) and (d) respectively. Comparing the reference and reconstructed real and imaginary parts of the complex permittivity of bone phantom P2, it can be observed that good reconstructions of bone dielectric properties are achieved by using DBIM based MWT imaging algorithm along with L_2-IMATCS approach.

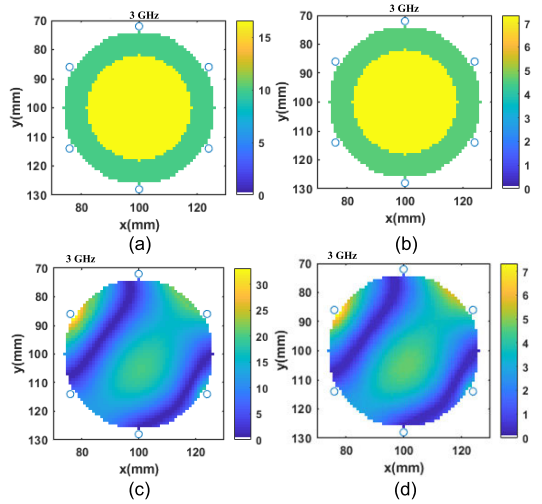

FIGURE 5. Real and imaginary parts of complex permittivity at 3 GHz of (a) and (b) reference bone phantom P2, (c) and (d) reconstructed bone phantom P2.

For the bone phantom P3, the internal layer of the 3-D printed calcaneus structure was filled with the liquid TMM of human osteoarthritis bone's TMM. The reference dielectric data for human osteoarthritis bone was obtained from Amin *et al.* [10]. The dielectric properties of osteoarthritis bones are higher as compared to osteoporotic bones. The contrast between dielectric properties of outer and inner layers of bone phantom P3 is higher compared to the bone phantoms P1 and P2. The reconstructed real and imaginary parts of the complex permittivity of bone phantom P3 are shown in Figure 6 (c) and (d) respectively. Comparing the reference and reconstructed real and imaginary parts of the complex permittivity parts of bone phantom P3, it can be observed that good reconstruction of experimental bone phantoms can be achieved by using DBIM and L_2-IMATCS approach, even for higher contrast two-layered bone phantom.

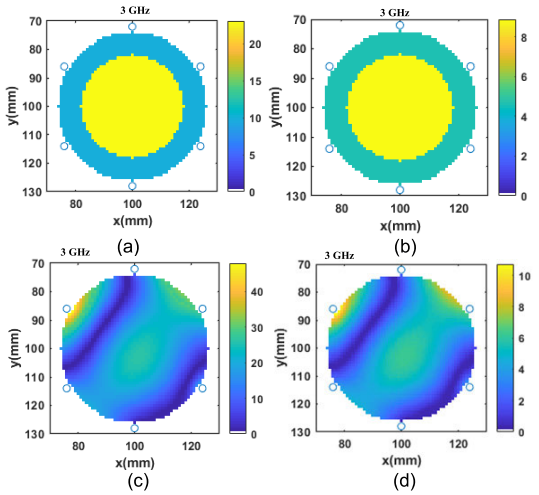

FIGURE 6. Real and imaginary parts of complex permittivity at 3 GHz of (a) and (b) reference bone phantom P3, (c) and (d) reconstructed bone phantom P3.

C. QUANTITATIVE EVALUATION OF RECONSTRUCTED PROFILES

To quantitatively evaluate the reconstructed bone phantoms P1, P2, and P3 this study has used NRMSE, SSIM, and histogram-based analysis. The results of NRMSE for real and imaginary parts of complex permittivity for all reconstructed bone phantoms are tabulated in Table 5. The lower error values of NRMSE for all reconstructed bone phantoms indicate the robustness of the L_2-IMATCS approach for the reconstruction of experimental data.

The results of SSIM between real and imaginary parts of reference and reconstructed complex permittivity profiles are tabulated in Table 5. Based on SSIM values in Table 5, it can be observed that the reference and reconstructed bone dielectric properties have high similarity in terms of real and imaginary parts of complex permittivity for each considered bone phantom. The values of NRMSE and SSIM for the real and imaginary parts of the complex permittivity as tabulated in Table 5 suggests that good reconstructions of bone dielectric properties can be achieved by using L_2-IMATCS approach.

TABLE 5. NRMSE and SSIM between original and reconstructed bone phantoms.

Phantom	NRMSE		SSIM	
	ε'	ε''	ε'	ε''
Normal Bone Phantom (P1)	0.456	0.637	0.963	0.920
Osteoporotic Bone Phantom (P2)	0.453	0.674	0.964	0.922
Osteoarthritis Bone Phantom (P3)	0.488	0.622	0.960	0.916

While NRMSE and SSIM do not evaluate the reconstructed images pixel-by-pixel which has paramount significance to evaluate the images in-depth, therefore, to address this limitation this study has proposed a novel histogram-based analysis. The histogram-based analysis computes the difference between all the corresponding reference and reconstructed pixels. The reconstructed image is classified as a better image if the majority of the pixels are centred at 0. Figure 7 (a), (b), and (c) represents the relative error distribution for the relative permittivity of bone phantoms P1, P2, and P3 respectively. The x-axis in the bar plot represents the difference between the relative permittivity of the reference and reconstructed relative permittivity and the y-axis represents the percentage of reconstructed pixels. It can be observed from Figure 7 (a), (b), and (c) that the majority of the reconstructed pixels have a low relative error. For bone phantoms, P1, P2, and P3 about 19.28%, 22%, and 17.44% of the reconstructed pixels respectively have relative error values close to 0. Furthermore, it can be observed from Figure 7 (a), (b), and (c) that few of the reconstructed pixels have non-zero error value due to non-uniform reconstruction of the imaging domain. This is because the MWI problem is inherently ill-posed and non-linear [39], therefore multiple solutions of the reconstruction domain exist. The reconstruction showed slightly large error values at the edges of the bone phantom and the interface between cortical bone and trabecular bone as can be seen in Figures 4, 5, and 6. The lower error values suggest that the reconstructed real part of the complex permittivity of bone phantoms P1, P2, and P3 can be achieved by using DBIM along with L_2-IMATCS approach.

D. CLASSIFICATION OF NORMAL AND DISEASED BONES BASED ON RECONSTRUCTED COMPLEX PERMITTIVITY PROFILES

An analysis has been performed to compare the peak values of the complex permittivity of reconstructed bone phantoms with the corresponding reference values. Figure 8(a) and (b) represents the comparison of the peak values of real and imaginary parts of the complex permittivity of bone phantoms P1, P2, and P3 respectively. The blue bars represent the peak value of the complex permittivity of the reference bone phantom, whereas, the brown bars represent the peak value of the reconstructed complex permittivity for each bone phantom. It can be observed from Figure 8 (a) and (b) that the differentiation between the different diseased bones is possible using the real part of the reconstructed complex permittivity of bone phantoms. Hence, the adopted approach for the differentiation of osteoporotic and osteoarthritis bone phantoms can be employed for bone health monitoring.

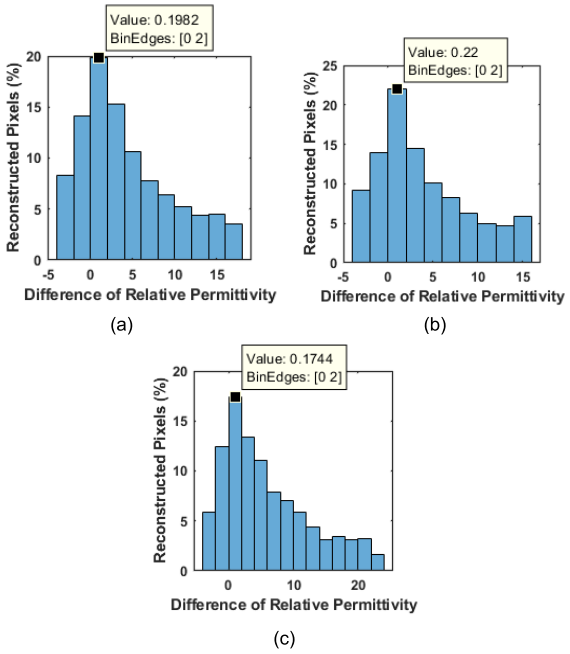

FIGURE 7. Distribution of reconstructed real part of complex permittivity of (a) bone phantom P1 (b) bone phantom P2 (c) bone phantom P3 at 3 GHz.

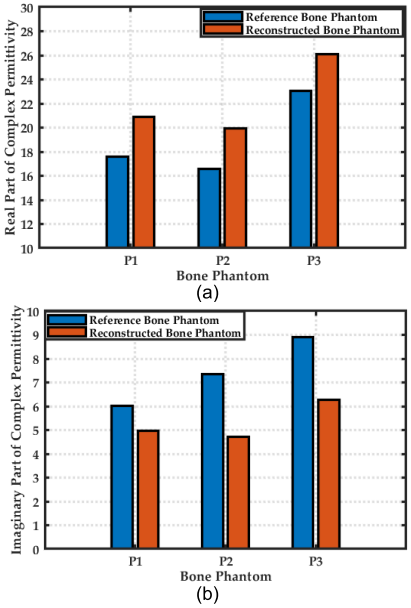

FIGURE 8. (a) Peak values of the real part of complex permittivity of reconstructed and reference bone phantoms (b) Peak values of the imaginary part of complex permittivity of reconstructed and reference bone phantoms at 3 GHz.

To avoid the possibility during the classification of normal and diseased bones that the detected peak value could be an artefact, this study has performed a histogram-based analysis to analyze the distribution of relative permittivity values of reconstructed pixels for the region of interest (central trabecular bone region) in the reconstructed image. Figure 9 (a), (b), and (c) represents the distribution of reconstructed relative permittivity for bone phantoms P1, P2, and P3 respectively. The x-axis in the bar plot represents the relative permittivity distribution and the y-axis represents the percentage of the reconstructed pixels. It can be observed from Figure 9 (a), (b), and (c) that the relative permittivity of the majority of the reconstructed pixels for each bone phantom is close to their corresponding reference values which ensures that the peak value used to classify normal and diseased bones is not an artefact. For bone phantom P1, P2, and P3 about 19.33%, 21.51%, and 16.45% of the reconstructed pixels respectively have values close to their respective reference values. The distribution of relative permittivity of each bone phantom compared to the reference profile ensures the robustness of L_2-IMATCS approach for the reconstruction of diverse bone phantoms. Hence, the adopted approach for the differentiation of osteoporotic and osteoarthritis bone phantoms can be employed for bone health monitoring.

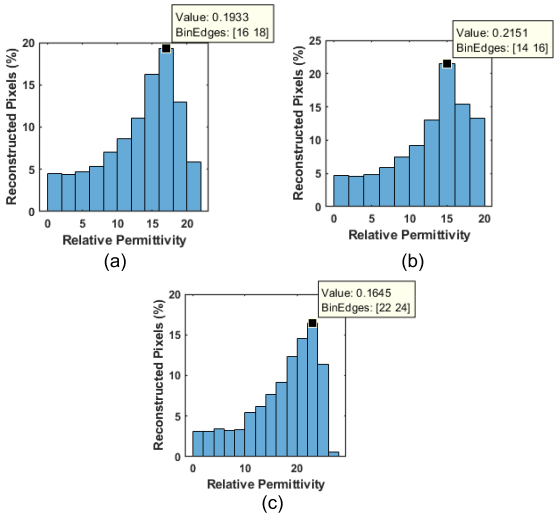

FIGURE 9. Distribution of reconstructed real part of complex permittivity of (a) bone phantom P1 (b) bone phantom P2 (c) bone phantom P3 at 3 GHz.

IV. CONCLUSION

The evaluation of the MWI prototype and imaging algorithms on experimental bone phantoms assists with assessing the robustness of the imaging approach for the reconstruction of dielectric properties under practical imaging situations. This study has presented the experimental evaluation of the MWI prototype designed to image a simplified calcaneus bone phantom. An equivalent simplified cylindrical model was used to mimic the shape of the human calcaneus bone. A dedicated MWI prototype was then presented to image the two-layered 3-D printed cylindrical calcaneus bone phantom. The external and internal layers of the cylindrical phantom were filled with liquid TMMs of cortical bone and trabecular bone respectively. A total of three bone phantoms with dielectric properties of different diseased human trabecular bones were developed. The TMMs were composed of Triton X-100, deionized water, and salt. The calcaneus bone phantom was placed in the MWI prototype and EM scattered waves were recorded at each antenna. To reconstruct the dielectric properties a DBIM based MWT approach is adopted in conjunction with L_2-IMATCS approach.

The results of reconstructed bone dielectric properties have shown that the adopted approach for linear inversion provides good reconstruction in comparison to the reference bone dielectric properties. The results have shown that the osteoporotic and osteoarthritis bones can be distinguished based on the reconstructed complex permittivity profiles. While the considered imaging scenario of a two-layered cylindrical-shaped bone phantom is rather anatomically simplistic, the study demonstrates the feasibility of reconstruction of bone dielectric properties using the proposed imaging method and the MWI prototype. Future work will focus on the estimation of dielectric properties of anatomically realistic bone phantoms that would also include skin, fat, and muscle layers by employing MWT to ultimately progress towards the measurement of *in vivo* dielectric properties of bone.

REFERENCES

[1] B. Amin, M. A. Elahi, A. Shahzad, E. Porter, B. McDermott, and M. O'Halloran, "Dielectric properties of bones for the monitoring of osteoporosis," *Med. Biol. Eng. Comput.*, vol. 57, no. 1, pp. 1–13, Aug. 2018.

[2] O. Johnell and J. A. Kanis, "An estimate of the worldwide prevalence and disability associated with osteoporotic fractures," *Osteoporosis Int.*, vol. 17, no. 12, pp. 1726–1733, Dec. 2006.

[3] S. N. Makarov, G. M. Noetscher, S. Arum, R. Rabiner, and A. Nazarian, "Concept of a radiofrequency device for osteopenia/osteoporosis screening," *Sci. Rep.*, vol. 10, no. 1, pp. 1–15, Dec. 2020.

[4] A. H. Golnabi, P. M. Meaney, S. Geimer, T. Zhou, and K. D. Paulsen, "Microwave tomography for bone imaging," in *Proc. IEEE Int. Symp. Biomed. Imag., Nano Macro*, Mar. 2011, pp. 956–959.

[5] E.-M. Lochmüller, R. Müller, V. Kuhn, C. A. Lill, and F. Eckstein, "Can novel clinical densitometric techniques replace or improve DXA in predicting bone strength in osteoporosis at the hip and other skeletal sites?" *J. Bone Mineral Res.*, vol. 18, no. 5, pp. 906–912, May 2003.

[6] B. Amin, A. Shahzad, D. Kelly, M. Ohalloran, and A. Elahi, "Anthropomorphic calcaneus phantom for microwave bone imaging applications," *IEEE J. Electromagn., RF Microw. Med. Biol.*, vol. 5, no. 3, pp. 206–213, Oct. 2020.

[7] B. Amin, A. Shahzad, L. Crocco, M. Wang, M. O'Halloran, A. González-Suárez, and M. A. Elahi, "A feasibility study on microwave imaging of bone for osteoporosis monitoring," *Med. Biol. Eng. Comput.*, vol. 59, no. 4, pp. 925–936, Apr. 2021.

[8] P. M. Meaney, T. Zhou, D. Goodwin, A. Golnabi, E. A. Attardo, and K. D. Paulsen, "Bone dielectric property variation as a function of mineralization at microwave frequencies," *Int. J. Biomed. Imag.*, vol. 2012, pp. 1–9, Jan. 2012.

[9] P. M. Meaney, D. Goodwin, A. H. Golnabi, T. Zhou, M. Pallone, S. D. Geimer, G. Burke, and K. D. Paulsen, "Clinical microwave tomographic imaging of the calcaneus: A first-in-human case study of two subjects," *IEEE Trans. Biomed. Eng.*, vol. 59, no. 12, pp. 3304–3313, Dec. 2012.

[10] B. Amin, A. Shahzad, L. Farina, E. Parle, L. McNamara, M. O'Halloran, and M. A. Elahi, "Dielectric characterization of diseased human trabecular bones at microwave frequency," *Med. Eng. Phys.*, vol. 78, pp. 21–28, Apr. 2020.

[11] P. M. Meaney, T. Zhou, D. Goodwin, A. Golnabi, E. A. Attardo, and K. D. Paulsen, "Bone dielectric property variation as a function of mineralization at microwave frequencies," *Int. J. Biomed. Imag.*, vol. 2012, pp. 1–9, Jan. 2012.

[12] D. O'Loughlin, M. O'Halloran, B. M. Moloney, M. Glavin, E. Jones, and M. A. Elahi, "Microwave breast imaging: Clinical advances and remaining challenges," *IEEE Trans. Biomed. Eng.*, vol. 65, no. 11, pp. 2580–2590, Nov. 2018.

[13] D. O'Loughlin, B. L. Oliveira, A. Santorelli, E. Porter, M. Glavin, E. Jones, M. Popovic, and M. O'Halloran, "Sensitivity and specificity estimation using patient-specific microwave imaging in diverse experimental breast phantoms," *IEEE Trans. Med. Imag.*, vol. 38, no. 1, pp. 303–311, Jan. 2019.

[14] M. Elahi, D. O'Loughlin, B. Lavoie, M. Glavin, E. Jones, E. Fear, and M. O'Halloran, "Evaluation of image reconstruction algorithms for confocal microwave imaging: Application to patient data," *Sensors*, vol. 18, no. 6, p. 1678, May 2018.

[15] E. Porter, M. Coates, and M. Popović, "An early clinical study of time-domain microwave radar for breast health monitoring," *IEEE Trans. Biomed. Eng.*, vol. 63, no. 3, pp. 530–539, Mar. 2016.

[16] R. C. Conceição, H. Medeiros, D. M. Godinho, M. O'Halloran, D. Rodriguez-Herrera, D. Flores-Tapia, and S. Pistorius, "Classification of breast tumor models with a prototype microwave imaging system," *Med. Phys.*, vol. 47, no. 4, pp. 1860–1870, Apr. 2020.

[17] A. H. Golnabi, P. M. Meaney, and K. D. Paulsen, "3D microwave tomography of the breast using prior anatomical information," *Med. Phys.*, vol. 43, no. 4, pp. 1933–1944, 2016.

[18] J. A. T. Vasquez, R. Scapaticci, G. Turvani, G. Bellizzi, D. O. Rodriguez-Duarte, N. Joachimowicz, B. Duchêne, E. Tedeschi, M. R. Casu, L. Crocco, and F. Vipiana, "A prototype microwave system for 3D brain stroke imaging," *Sensors*, vol. 20, no. 9, pp. 1–16, 2020.

[19] S. Ahsan, Z. Guo, Z. Miao, and I. Sotiriou, M. Koutsoupidou, E. Kallos, G. Palikaras, and P. Kosmas, "Design and experimental validation of a multiple-frequency microwave tomography system employing the DBIM-TwIST algorithm," *Sensors*, vol. 18, no. 10, p. 3491, 2018.

[20] O. Karadima, M. Rahman, I. Sotiriou, N. Ghavami, P. Lu, S. Ahsan, and P. Kosmas, "Experimental validation of microwave tomography with the DBIM-TwIST algorithm for brain stroke detection and classification," *Sensors*, vol. 20, no. 3, p. 840, Feb. 2020.

[21] S. Ahsan, Z. Guo, Z. Miao, I. Sotiriou, M. Koutsoupidou, E. Kallos, G. Palikaras, and P. Kosmas, "Design and experimental validation of a multiple-frequency microwave tomography system employing the DBIM-TwIST algorithm," *Sensors*, vol. 18, no. 10, p. 3491, Oct. 2018.

[22] B. Amin, A. Shahzad, M. O'halloran, and M. A. Elahi, "Microwave bone imaging: A preliminary investigation on numerical bone phantoms for bone health monitoring," *Sensors*, vol. 20, no. 21, pp. 1–21, 2020.

[23] C. Gilmore, A. Zakaria, S. Pistorius, and J. LoVetri, "Microwave imaging of human forearms: Pilot study and image enhancement," *Int. J. Biomed. Imag.*, vol. 2013, pp. 1–17, Aug. 2013.

[24] B. Amin, D. Kelly, A. Shahzad, M. O'Halloran, and M. A. Elahi, "Microwave calcaneus phantom for bone imaging applications," in *Proc. 14th Eur. Conf. Antennas Propag. (EuCAP)*, Mar. 2020, pp. 1–5.

[25] N. Joachimowicz, B. Duchêne, C. Conessa, and O. Meyer, "Anthropomorphic breast and head phantoms for microwave imaging," *Diagnostics*, vol. 8, no. 4, p. 85, Dec. 2018.

[26] J. Bourqui, J. M. Sill, and E. C. Fear, "A prototype system for measuring microwave frequency reflections from the breast," *Int. J. Biomed. Imag.*, vol. 2012, pp. 1–12, Jan. 2012.

[27] T. Rydholm, A. Fhager, M. Persson, S. Geimer, and P. Meaney, "Effects of the plastic of the realistic GeePS-L2S-Breast phantom," *Diagnostics*, vol. 8, no. 3, p. 61, Sep. 2018.

[28] L. M. Neira, B. D. Van Veen, and S. C. Hagness, "High-resolution microwave breast imaging using a 3-D inverse scattering algorithm with a variable-strength spatial prior constraint," *IEEE Trans. Antennas Propag.*, vol. 65, no. 11, pp. 6002–6014, Nov. 2017.

[29] C. Gilmore, P. Mojabi, and J. LoVetri, "Comparison of an enhanced distorted born iterative method and the multiplicative-regularized contrast source inversion method," *IEEE Trans. Antennas Propag.*, vol. 57, no. 8, pp. 2341–2351, Aug. 2009.

[30] P. Kosmas and F. Marvasti, "Microwave medical imaging based on sparsity and an iterative method with adaptive thresholding," *IEEE Trans. Med. Imag.*, vol. 34, no. 2, pp. 357–365, Sep. 2014.

[31] R. Scapaticci, P. Kosmas, and L. Crocco, "Wavelet-based regularization for robust microwave imaging in medical applications," *IEEE Trans. Biomed. Eng.*, vol. 62, no. 4, pp. 1195–1202, Apr. 2015.

[32] M. Ambrosanio, P. Kosmas, and V. Pascazio, "A multithreshold iterative DBIM-based algorithm for the imaging of heterogeneous breast tissues," *IEEE Trans. Biomed. Eng.*, vol. 66, no. 2, pp. 509–520, Feb. 2019.

[33] A. Shahzad, M. O'Halloran, E. Jones, and M. Glavin, "A multistage selective weighting method for improved microwave breast tomography," *Computerized Med. Imag. Graph.*, vol. 54, pp. 6–15, Dec. 2016.

[34] J. M. Vogel, R. D. Wasnich, and P. D. Ross, "The clinical relevance of calcaneus bone mineral measurements: A review," *Bone Mineral*, vol. 5, no. 1, pp. 35–58, Oct. 1988.

[35] B. Clarke, "Normal bone anatomy and physiology," *Clin. J. Amer. Soc. Nephrol.*, vol. 3, no. 3, pp. 1–16, 2008.

[36] B. L. Oliveira and M. O. Halloran, "Microwave breast imaging: Experimental tumour phantoms for the evaluation of new breast cancer diagnosis systems," *Biomed. Phys. Eng. Exp.*, vol. 4, no. 2, Jan. 2018, Art. no. 025036.

[37] S. Salahuddin, E. Porter, F. Krewer, and M. O' Halloran, "Optimised analytical models of the dielectric properties of biological tissue," *Med. Eng. Phys.*, vol. 43, pp. 103–111, May 2017.

[38] C. Gabriel and A. Peyman, "Dielectric measurement: Error analysis and assessment of uncertainty," *Phys. Med. Biol.*, vol. 51, no. 23, pp. 6033–6046, Dec. 2006.

[39] J. D. Shea, P. Kosmas, S. C. Hagness, and B. D. Van Veen, "Three-dimensional microwave imaging of realistic numerical breast phantoms via a multiple-frequency inverse scattering technique," *Med. Phys.*, vol. 37, no. 8, pp. 4210–4226, Aug. 2010.

[40] Y. M. Wang, "Reconstruction of two-dimensional permittivity distribution using the distorted Born iterative method," *IEEE Trans. Med. Imag.*, vol. 9, no. 2, pp. 218–225, Jun. 1990.

[41] R. Scapaticci, M. Bjelogrlic, J. A. T. Vasquez, F. Vipiana, M. Mattes, and L. Crocco, "Microwave technology for brain imaging and monitoring: Physical foundations, potential and limitations," in *Emerging Electromagnetic Technologies for Brain Diseases Diagnostics, Monitoring and Therapy*. Cham, Switzerland: Springer, 2018, pp. 7–35.

[42] A. Fhager, S. K. Padhi, and J. Howard, "3D image reconstruction in microwave tomography using an efficient FDTD model," *IEEE Antennas Wireless Propag. Lett.*, vol. 8, pp. 1353–1356, 2009.

[43] R. Ciocan and H. Jiang, "Model-based microwave image reconstruction: Simulations and experiments," *Med. Phys.*, vol. 31, no. 12, pp. 3231–3241, Nov. 2004.

[44] R. Scapaticci, P. Kosmas, and L. Crocco, "Wavelet-based regularization for robust microwave imaging in medical applications," *IEEE Trans. Biomed. Eng.*, vol. 62, no. 4, pp. 1195–1202, Apr. 2015.

[45] C. Gabriel, R. W. Lau, and C. Gabriel, "The dielectric properties of biological tissues: III. Parametric models for the dielectric spectrum of tissues," *Phys. Med. Biol.*, vol. 41, no. 11, p. 2271, 1996.

[46] B. McDermott, E. Porter, A. Santorelli, B. Divilly, L. Morris, M. Jones, B. McGinley, and M. O'Halloran, "Anatomically and dielectrically realistic microwave head phantom with circulation and reconfigurable lesions," *Prog. Electromagn. Res. B*, vol. 78, pp. 47–60, (Aug). 2017.

[47] B. L. Oliveira, D. O'Loughlin, M. O'Halloran, E. Porter, M. Glavin, and E. Jones, "Microwave breast imaging: Experimental tumour phantoms for the evaluation of new breast cancer diagnosis systems," *Biomed. Phys. Eng. Exp.*, vol. 4, no. 2, p. 25036, 2018.

BILAL AMIN received the B.S. degree (Hons.) in electrical engineering from COMSATS University Lahore, Pakistan, in 2013, under the auspices of the National ICT Scholarship Program, the master's degree in electrical engineering from COMSATS University Islamabad, Pakistan, and the Ph.D. degree in electrical and electronics engineering from the National University of Ireland, Galway. He is currently a Postdoctoral Researcher with the School of Medicine, National University of Ireland, Galway. His current research interests include compressive sampling, microwave imaging, medical signal processing, dielectric metrology, bone health monitoring, and electromagnetic medical systems.

ATIF SHAHZAD received the B.S. degree (Hons.) in computer engineering from COMSATS University Lahore, the M.Sc. degree in electronic engineering from the University of Leeds, and the Ph.D. degree in medical engineering from the National University of Ireland, Galway, in 2006, 2009, and 2015, respectively. He is currently a Research Lecturer in medical technologies and the Co-Director of the Smart Sensors Laboratory, National University of Ireland, Galway. His research interests include medical sensing technologies, device development, signal and image processing, and artificial intelligence in healthcare. He has received over 13 national and international awards, including Presidential Award for Distinguished Achievers.

MARTIN O'HALLORAN is currently a Professor in medical electronics and a Science Foundation Ireland (SFI) Investigator with the National University of Ireland, Galway. Reflecting the interdisciplinary nature of his research, he holds a joint affiliation with the College of Engineering and Informatics; and the College of Medicine, Nursing & Health Sciences, and leads the Translational Medical Device Laboratory, Lambe Institute. He has received over 30 national and international research awards and was recently awarded SFI's Early-Stage Researcher of the Year, Engineers Ireland Chartered Engineer of the Year, and the European Research Council's Starting Investigator Grant. He was a Co-Proposer of an European COST Action (entitled ''MiMED'') and is now leading a network of over 180 medical device researchers from 24 countries, focused on the clinical evaluation and commercialization of novel medical devices in Europe. Over the last six years, he has personally secured €5.6 million in direct research funding and has published more than 40 articles in peer-reviewed journals. He has been an invited chair and an invited speaker at several major electromagnetics and translational medicine conferences/seminars. He is currently a Non-Executive Director of the BioInnovate Program and the Co-Lead of the Health Innovation Hub Ireland, NUI Galway.

BARRY MCDERMOTT received the Ph.D. degree in medical device engineering and Professional Level degree in engineering, pharmacy and veterinary medicine. He is currently a Senior Research Fellow with the School of Medicine, National University of Ireland, Galway. His research interests include the use of impedance imaging applied to clinical problems, but he also actively works on the development of innovative therapeutics for conditions, such as osteoarthritis, and particularly, he is interested in the interface between drugs and devices.

ADNAN ELAHI (Member, IEEE) received the B.S. degree in computer engineering from COMSATS University Lahore, Pakistan, the M.Sc. degree in embedded digital systems from the University of Sussex, U.K., and the Ph.D. degree in electronic engineering from the National University of Ireland, Galway. He is currently a Lecturer in medical electronics with the National University of Ireland, Galway. His Ph.D. research was focused on the investigation and development of novel signal processing algorithms to improve microwave imaging of the breast. His research spans the disciplines of engineering and medicine, with a particular focus on smart devices for chronic disease management; novel and personalized therapeutics using electroporation and neurostimulation; and AI/machine learning for biomedical signals. Previously, he has worked as a Lecturer with COMSATS University Lahore and as a Research Associate with the Computer Vision Research Group (COMVIS), Lahore, Pakistan.